CHAPTER - 6
DIELECTRIC RELAXATION OF $NiFe_2O_4/Gd_2O_3$ CORE-SHELL NANOPARTICLES

6.1 Introduction

Nanoparticles having core-shell structure are the subject of the investigation in recent years and may be an interesting material for the technological applications [1]. They possess unique physical and chemical properties [2, 3] which can be tuned by changing the chemical composition as well as the size of the core and shell [4-7]. The technological application of any material depends upon its dielectric properties. The polycrystalline ferrites are very good dielectric materials. Younas *et al*.[8] have investigated the dielectric properties of $NiFe_2O_4$ and observed a semiconducting to metallic transition at 358 K due to the transition from localized charge carrier [Fe^{3+}-O^{2-}-Fe^{3+}]/[Ni^{2+}-O^{2-}-Ni^{2+}] linkage to delocalized charge carrier [Fe^{3+}-Fe^{2+}]/[Ni^{2+}-Ni^{3+}] linkage. This may be possible because, in the process of preparation of ferrites, under slightly reduced conditions, the divalent iron formed in the body of the ferrite material leads to high conducting grains. When such materials are cooled in an oxygen atmosphere, it is possible to form layers of very low conductivity over its constituent grains. Almost all the ferrites in the polycrystalline form have relatively high conducting grains separated by low conducting layers, so that they behave as a homogeneous dielectric material [9]. Grain size effect and processing route in the synthesis of ferrites have been found to have relationship among power loss, low eddy current losses and better magnetic properties. Small grain size has given rise to the low power loss and this is attributed to unique uniformity and higher chemical homogeneity and grain uniformity in Mn–Zn ferrites [10]. Recently, dielectric studies of gadolinium oxide (Gd_2O_3) NPs have been of research interest because of its high

dielectric constant and charge storage capacitance [11-13].

In the present work, we have investigated the dielectric properties of Gd_2O_3 encapsulated $NiFe_2O_4$ core-shell nanoparticles (CSNPs) because the crystal phases of the core material can be stabilized by the shell material to some extent. Lin *et al*. [14] have investigated the dielectric properties of core-shell structured nickel oxide based ceramics and shown that the concentration of shell materials has a remarkable effect on the dielectric properties of the core materials. Using alternating current impedance spectroscopy (AICS), we have investigated the dielectric relaxation of $NiFe_2O_4/Gd_2O_3$ CSNPs in a wide temperature and frequency range.

6.2 Experimental Procedure

$Gd(NO_3)_3.6H_2O$ (Alfa Aesar), $Ni(NO_3)_2.6H_2O$ (Alfa Aesar) and $FeCl_3$ (Merck) were used as starting materials and polyethylene glycol 400 (PEG) was used as solvent. We have used the chemical method to synthesize $NiFe_2O_4$ core followed by nucleation and growth of Gd_2O_3 shell on the core particles.

For the synthesis of $NiFe_2O_4$, 4 mM of $Ni(NO_3)_2.6H_2O$ and 8 mM of $FeCl_3$ were dissolved in 30 ml of PEG under stirring at 100 $^{\circ}$C. The clear transparent salt solution was subsequently heated to 180 $^{\circ}$C for 90 min. The resulting reddish brown solution of $NiFe_2O_4$ was cooled down to room temperature, diluted with ethanol and the NPs were separated from the solution by centrifugation at 10,000 rpm. For the synthesis of Gd_2O_3 NPs, 12 mM of $Gd(NO_3)_3.6H_2O$ was dissolved in 30 ml of PEG under stirring at 100 $^{\circ}$C, subsequently heated to 180 $^{\circ}$C for 90 min and finally cooled down to room temperature. The brown suspension of Gd_2O_3 was diluted with ethanol and the NPs were separated from the solutions by centrifugation at 10,000 rpm. To remove any unreacted precursor and PEG, the sediment materials were dispersed in ethanol and centrifuged for several times. The materials obtained after centrifugation

were calcined at 600 $^{\circ}$C for 2 h in air.

To get the NPs of $NiFe_2O_4/Gd_2O_3$ core-shell, Gd_2O_3 shell was grown on the $NiFe_2O_4$ core employing a two-step process. Firstly, the as-prepared $NiFe_2O_4$ core NPs were dispersed in 25 ml of PEG under sonication for 10 min and then a solution of PEG (15 ml) containing 12 mM of $Gd(NO_3)_3.6H_2O$ was injected into the dispersed nano-core system. After mixing the above solution (using a magnetic stirrer for 15 min), the mixed system was heated at 180 $^{\circ}$C for 2 h and cooled down to room temperature, washed, centrifuged and after that calcined at 600 $^{\circ}$C for 2 h in air to get $NiFe_2O_4/Gd_2O_3$ CSNPs. The phase purity and crystal structure of the synthesised samples were analysed by powder XRD (Rigaku Miniflex-II) at room temperature. The mirco-structural investigation of the CSNPs was done using TEM TecnaiTM G^2 F30 S-TWIN operating at 300 kV. Sample for TEM was prepared by placing a drop of colloidal acetone solution of the powder sample onto a carbon coated Cu grid and the grid was dried in air. The UV-Visible absorption spectrum of CSNPs was measured using UV-Visible spectrophotometer (Shimadzu UV-2401). The impedance, phase factor, capacitance and conductance of the sample were measured using an LCR meter (HIOKI) in the frequency range from 50 Hz to 1.1 MHz at the oscillation voltage of 1.0 V. The measurements were performed over the temperature range from room temperature (303 K) to 543 K using an inbuilt cooling-heating system. Each measured temperature was kept constant with an accuracy of ±1 K. The complex electric modulus M^* (= $1/\varepsilon^*$) and the ac electrical conductivity σ (= $\omega\varepsilon_o\varepsilon''$) were obtained from the temperature dependence of the real (ε') and imaginary (ε'') components of the complex dielectric constant ε^* (= $\varepsilon' - j\varepsilon''$).

6.3 Results and Discussion

6.3.1 Structural and Micrographical Studies

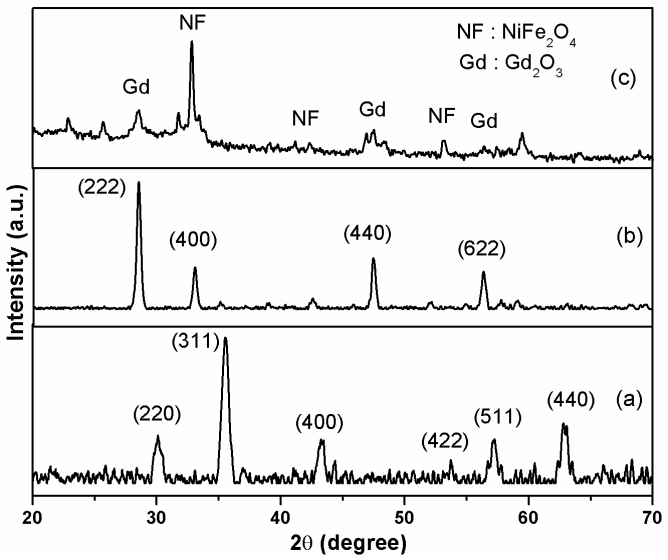

Figure 6.1 X-ray diffraction patterns of (a) $NiFe_2O_4$, (b) Gd_2O_3 and (c) $NiFe_2O_4/Gd_2O_3$ NPs

The XRD patterns of $NiFe_2O_4$, Gd_2O_3 and $NiFe_2O_4/Gd_2O_3$ CSNPs are shown in Figure 6.1. In the XRD pattern of $NiFe_2O_4$ NPs (Figure 6.1a) the major peaks are at $2\theta = 30.12^{\circ}$, 35.56° and 63.08° corresponding to (220), (311) and (440) crystal planes and this diffraction pattern is well matched with JCPDS data (card number 10-0325). The XRD pattern of Gd_2O_3 NPs (Figure 6.1b) shows the existence of strong and sharp diffraction peaks at $2\theta = 28.50^{\circ}$, 33.06°, 47.44° and 56.34° corresponding to its crystal planes are (222), (400), (440) and (622) respectively. The nature and position of the above diffraction peaks are characteristic of cubic gadolinium oxide phase as cited in other reports [15] and JCPDS data (card number 43-1014). The diffraction pattern of $NiFe_2O_4/Gd_2O_3$ CSNPs (Figure 6. 1c) shows the existence of diffraction peaks of both core and shell materials where the peak positions are slightly shifted compared to their bare diffraction pattern. The observed shift in the diffraction angle may be due to the strain growth of shell material on the core. Cao and Banin reported that the

diffraction peaks shift to higher 2θ angles because of the strain from epitaxial growth of an InP shell on an InAs core [16]. Nickel ferrite core has a smaller lattice constant compared to the gadolinium oxide shell. Due to this lattice mismatch, there is a chance of overlapping the diffraction peaks of these two materials particularly between the diffraction angle $2\theta = 35.5_{(core)}$ and $35.12_{(shell)}$. The gadolinium oxide shell will experience the strain during the epitaxial growth on the surface of core material which causes the shift in the diffraction peak angle from their original position.

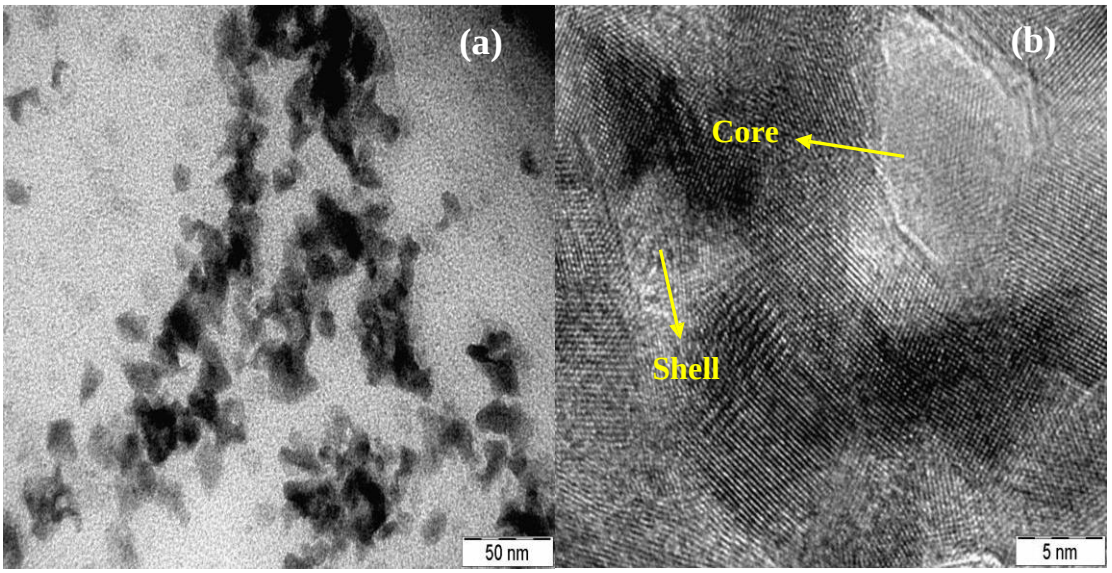

Figure 6.2 (a) TEM micrograph obtained for $NiFe_2O_4/Gd_2O_3$ CSNPs and (b) HRTEM micrograph for the single CSNP

The TEM micrograph of $NiFe_2O_4/Gd_2O_3$ CSNPs is shown in Figure 6.2 where the core material darker part is encapsulated by shell. The overall particle size is found to be ~ 60 nm. The HRTEM image of single CSNP (Figure 6.2b) shows the different crystalline lattice directions for core and shell materials which further confirm the core-shell structure of the prepared sample.

6.3.2 Optical Studies

Figure 6.3 shows the UV-Visible absorption spectrum of $NiFe_2O_4/Gd_2O_3$ CSNPs. The optical band gap energy (E_g) is estimated by the method proposed by Wood and Tauc [17]. The optical band gap is associated with absorbance and photon energy by the following relation:

$$\alpha h\nu = A(h\nu - E_g)^n \quad \ldots\ldots\ldots\ldots\ldots\ldots (6.1)$$

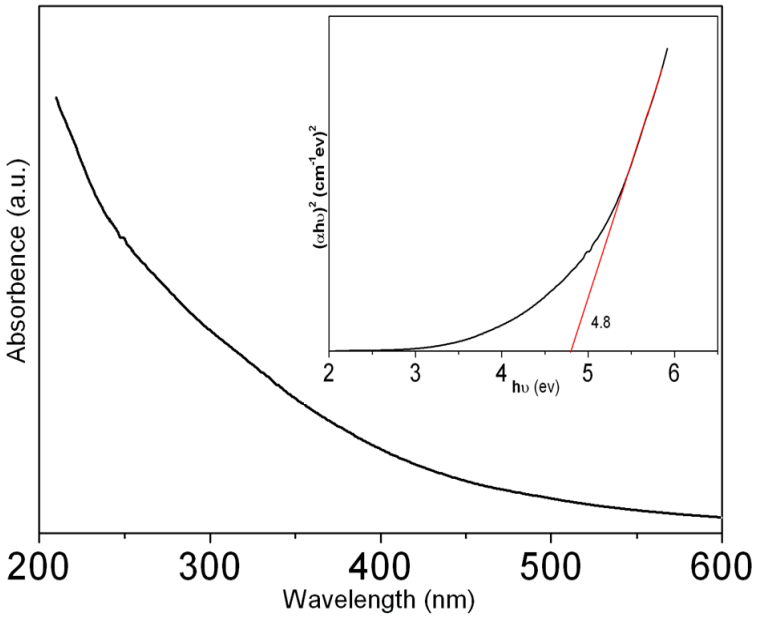

Figure 6.3 UV-Visible absorbance spectrum of $NiFe_2O_4/Gd_2O_3$ CSNPs, $(\alpha h\nu)^2$ *vs* $h\nu$ graph is shown in the inset

where α is the absorption coefficient, h is the Plank‟s constant, ν is the frequency, E_g is the optical band gap and n is a constant associated to the different types of electronic transitions (n = 1/2, 2, 3/2 or 3 for direct allowed, indirect allowed, direct forbidden and indirect forbidden transitions respectively). According to Liu *et al.* [18], the oxides are characterised by a direct allowed electronic transition and hence, the n = 1/2 value is used as standard in Eq. (6.1). Thus, the E_g values have been evaluated by extrapolating the linear portion of the $(\alpha h\nu)^2$ curve to the $h\nu = 0$ axis as shown in inset of Figure 6.3. The obtained optical band gap energy for

$NiFe_2O_4/Gd_2O_3$ CSNPs is found to be 4.8 eV which lies in between the individual band gap of Gd_2O_3 (~ 5 - 5.6 eV) [19] and $NiFe_2O_4$ (~ 2.7 eV) [20].

6.3.3 Dielectric Relaxation

The angular frequency ($\omega = 2\pi\nu$) dependence of the real part (ε') of complex dielectric constant (ε^*) and the dielectric loss tangent ($\tan\delta$) of $NiFe_2O_4/Gd_2O_3$ at various temperatures is shown in Figures 6.4a and 6.4b respectively. A relaxation is observed in the entire temperature range as a gradual decrease in ε' and as a broad peak in $\tan\delta$. Relaxation phenomena in dielectric materials are associated with a frequency-dependent orientational polarization. At low frequency, the permanent dipoles align themselves along the field and contribute fully to the total polarization of the dielectric. At higher frequency, the variation in the field is too rapid for the dipoles to align themselves, so their contribution to the polarization and hence to the dielectric permittivity can become negligible. Therefore, the dielectric permittivity ε' decreases with increasing frequency. The decrease in ε' is accompanied by a peak in $\tan\delta$, which also shifts to higher frequency on increasing the temperature as shown in Figure 6.4b. Hence, it is tentatively concluded that, at higher temperature, the rate of polarization is high and thus the relaxation occurs at a high frequency. The high value of ε' at frequencies lower than 1 kHz which increases with increasing temperature may be attributed to free charge buildup at the interface between the core and the shell of the materials. The dielectric constant of $NiFe_2O_4$ at room temperature is found to be 1100 at 100 Hz [8]. The same is not observed for the present system because Gd_2O_3 has modulated the dielectric properties of $NiFe_2O_4$. The dielectric constant of $NiFe_2O_4/Gd_2O_3$ CSNPs at room temperature is only 250 at 100 Hz. It is to be mentioned that Younas *et al*.[8] have observed a semiconducting to metallic transition at 358 K in $NiFe_2O_4$ due to the transition from localized charge carrier [Fe^{3+}-O^{2-}-

Fe^{3+}]/[Ni^{2+}-O^{2-}-Ni^{2+}] linkage to delocalized charge carrier [Fe^{3+}-Fe^{2+}]/[Ni^{2+}-Ni^{3+}] linkage. Such behaviour is not observed in the present CSNPs. Because of the shell material coating, the thermal stability of the core particle can be modified, so that the overall particle stability of the core particle has increased.

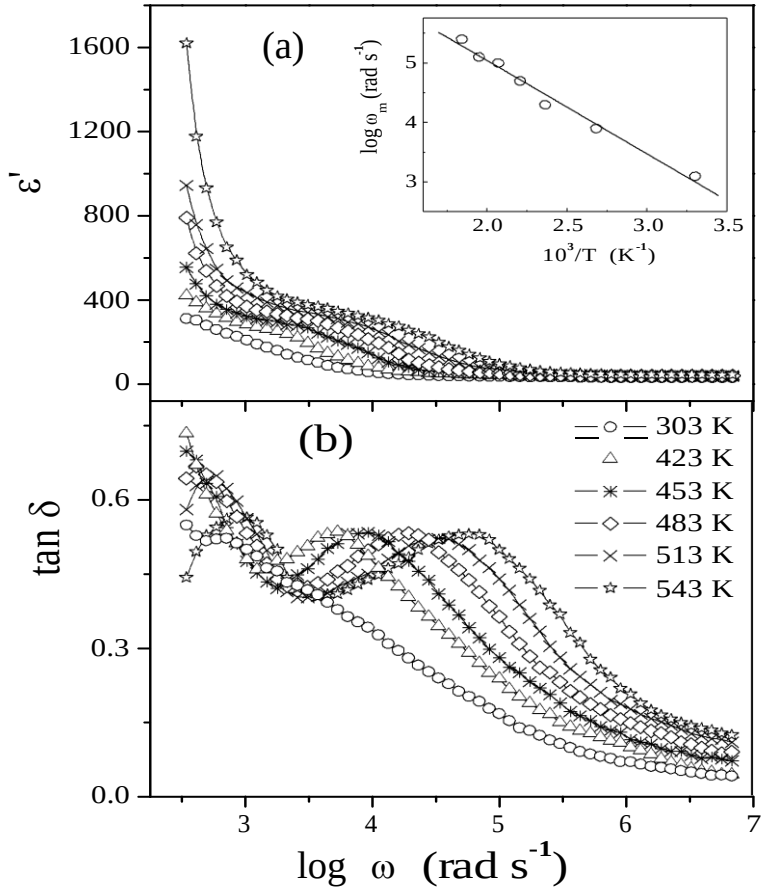

Figure 6.4 Angular frequency ($\omega = 2\pi\nu$) dependence plots of (a) the real part (ε') of complex dielectric constant and (b) the dielectric loss tangent ($\tan\delta$) of $NiFe_2O_4/Gd_2O_3$ at various temperatures. Temperature dependence of the characteristic relaxation time is shown in the inset of Figure 6.4a

For the measurement of the characteristic relaxation time (η_m), one can choose the inverse of frequency of the peak position in $\tan\delta$ versus $\log\omega$ plots in Figure 6.4b, i.e., $\eta_m = \omega_m^{-1}$. The temperature dependence of the characteristic relaxation time is shown in the inset of Figure 6.4a, which satisfies the Arrhenius law given as

$$\omega_m = \omega_0 \exp\left[-\frac{E_a}{K_B T}\right] \quad \ldots\ldots\ldots\ldots\ldots\ldots\ldots\ldots \quad (6.2)$$

where ω_m is the angular frequency corresponding to peak maximum, ω_0 is the pre exponential factor, E_a is the activation energy required for dielectric relaxation, T is the measuring temperature and K_B is the Boltzmann constant. From the numerical fitting analysis, we have obtained the value of the activation energy = 0.3 eV. Such a value of activation energy suggests an electronic conduction mechanism for dielectric relaxation of $NiFe_2O_4/Gd_2O_3$ CSNPs.

6.3.4 Complex Impedance

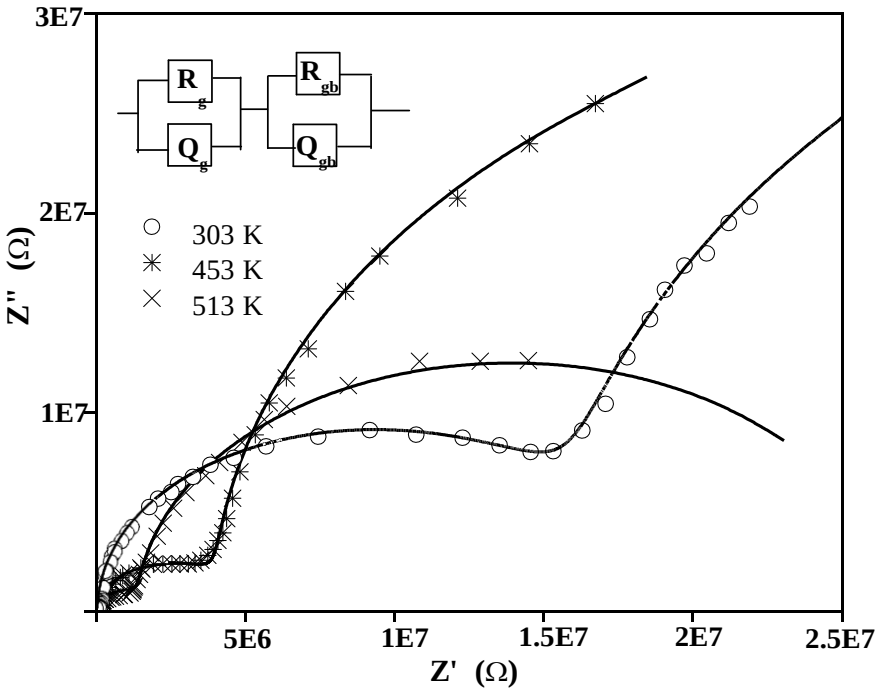

Figure 6.5 Complex impedance plane plots at different temperatures for $NiFe_2O_4/Gd_2O_3$ CSNPs

Figure 6.5 shows the complex impedance plane plots (Nyquist plots) at different temperatures for $NiFe_2O_4/Gd_2O_3$ CSNPs. The presence of two well resolved arcs at each temperature indicates the presences of two types of relaxation process with sufficiently different relaxation time in the sample. It has been observed from Figure 6.5 that the grain contribution is shifted to the higher frequency side and grain boundary dominants over the grain contribution with the increase of temperature. The

effect of grain and grain-boundary contributions in the material can be separated by fitting the experimental response to that of an electrical equivalent circuit, which is usually considered to comprise a series of two parallel resistor–capacitor (R–C) elements. One branch is associated with the grain and other with the grain-boundary effect of the sample. Due to the non-ideal behaviour of the capacitance, sometimes both grain and grain-boundary contributions though small are present in a same frequency range which may give rise to the depressed arcs or even only a spike like nature at low frequency side with a small arc at high frequency region in complex impedance plane plot. For such cases, the capacitance term in RC-equivalent circuit is replaced by a constant phase element (CPE).

The capacitance of CPE can be expressed as $C_{CPE} = Q^{1/k}R^{(1-k)/k}$, where k estimates the non-ideal behaviour for grain (k_g) and grain boundary (k_{gb}). The value of k is zero for ideal resistance and 1 for ideal capacitance. Here R and Q are the resistance and the constant phase element (CPE) for grain interiors (R_g, Q_g) and grain boundaries (R_{gb}, Q_{gb}) respectively. The solid lines in Figure 6.5 represent the fitting of electrical equivalent circuit as shown in the inset and the fitted parameters are listed in Table 6.1. The decrease in the resistance of grains and grain-boundaries with increasing temperature suggests the semiconducting nature of $NiFe_2O_4/Gd_2O_3$ CSNPs. The decrease of grain resistance with temperature is shown in Figure 6.6.

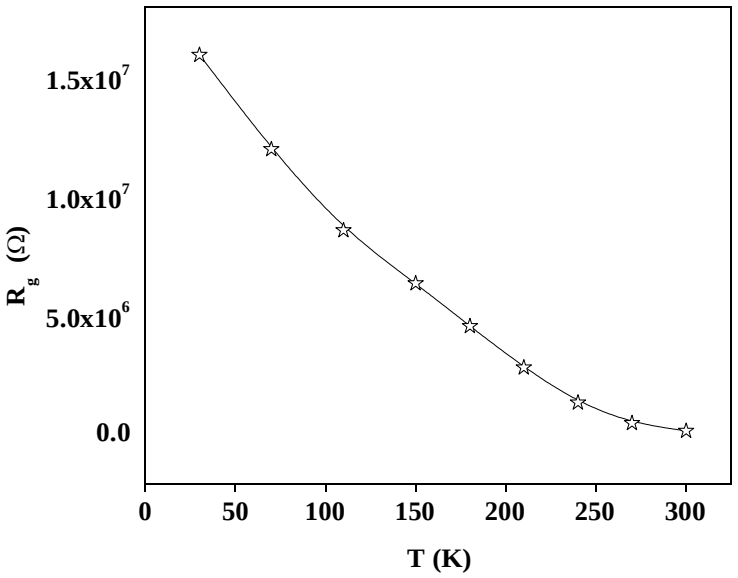

Figure 6.6 Temperature dependence of R_g

Table 6.1 Various fitting parameters for Nyquist impedance plots

Temperature K	R_g Ω	Q_g F/mΩ	k_g	R_{gb} Ω	Q_{gb} F/mΩ	k_{gb}
303	$1.6x10^7$	$6x10^{-10}$	0.5	$7.4x10^7$	$2.3x10^{-9}$	0.35
453	$4.0x10^6$	$7.8x10^{-10}$	0.56	$6.4x10^7$	$2.4x10^{-9}$	0.36
513	$1.4x10^6$	$8.0x10^{-10}$	0.6	$2.5x10^7$	$2.7x10^{-9}$	0.40

6.3.5 Electric Modulus

The electric modulus corresponds to the relaxation of the electric field in the materials when the electric displacement remains constant. The relaxation mechanism in the electric modulus formalism is studied by plotting the imaginary modulus (M″) as a function of frequency at various temperatures, where peaks are observed in the plot corresponding to a relaxation process and the peak height is inversely proportional to the capacitance of the sample. Figure 6.7 displays the frequency (angular) dependence of M″ for $NiFe_2O_4/Gd_2O_3$ CSNPs as a function of temperature, where the relaxation peak moves towards lower frequencies during cooling of the

sample. Consequently, it means that the relaxation rate for the process decreases with decrease in temperature. The relaxation mechanism can be modelled by Cole–Cole [21] or Davidson–Cole [22] or Havriliak–Negami [23] equations. Due to the asymmetric nature of M″ peaks, we have fitted our experimental data as shown by solid lines in Figure 6.7 with the Havriliak–Negami expression defined as [24],

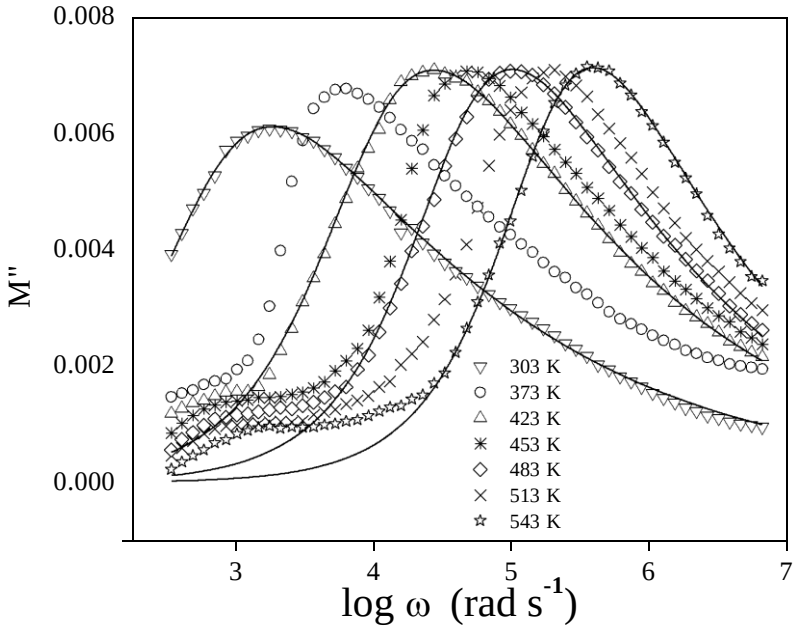

Figure 6.7 Frequency dependence of M″ for $NiFe_2O_4/Gd_2O_3$ CSNPs as a function of temperature

$$M'' = \frac{M_\infty M_s[(M_\infty - M_s)\sin\gamma\varphi]A^\gamma}{M_s^2 A^{2\gamma} + 2A^\gamma(M_\infty - M_s)M_s\cos\gamma\varphi + (M_\infty - M_s)^2} \quad \text{.....(6.3)}$$

Where,

$$A = \left[1 + 2(\omega\tau)^{1-\alpha}\sin(\alpha\pi/2) + (\omega\tau)^{2(1-\alpha)}\right]^{1/2}$$

and

$\phi = \tan^{-1}[(\omega\tau)^{1-\alpha}]\cos(\alpha\pi/2)1+(\omega\tau)^{1-\alpha}\sin(\alpha\pi/2)]$

The values of γ lie in between 0.32 and 0.45 and α varies from 0.85 to 0.93 for the temperature range from 303 K to 543 K. These values indicate that the relaxation process is poly-dispersive in nature for which parameters γ and α vary between 0 and 1 [25]. The value of γ is 1 and α is 0 for mono-dispersive Debye process. The parameter α is often used to describe the divergence of a measured dielectric dispersion from the ideal dispersion exhibited by a Debye type of dielectric relaxation and is widely assumed to be related to a distribution of the relaxation times in the system.

6.3.6 AC Conductivity

In order to understand the dynamics of the charge carriers and the effect of conductivity on the dielectric properties of $NiFe_2O_4/Gd_2O_3$ CSNPs, the frequency dependence of ac conductivity in the temperature range from 303 K to 543 K is shown in Figure 6.8. The conductivity plots can be conveniently divided into two frequency regions: (i) from 50 to $4x10^3$ Hz and (ii) from $2x10^4$ to 10^6 Hz. The frequency dependent ac conductivity plots are well described by the double power law given as [26]

$$\sigma_1(\omega) = \sigma_0 + A_1\,\omega^{s1} + A_2\,\omega^{s2} \quad \text{..... (6.4)}$$

where, the exponents s1 and s2 characterise the low frequency and the high frequency regions respectively. The solid lines in the Figure 6.8 represent the fitting of Eq. (6.4) with experimental data at 543 K and 423 K.

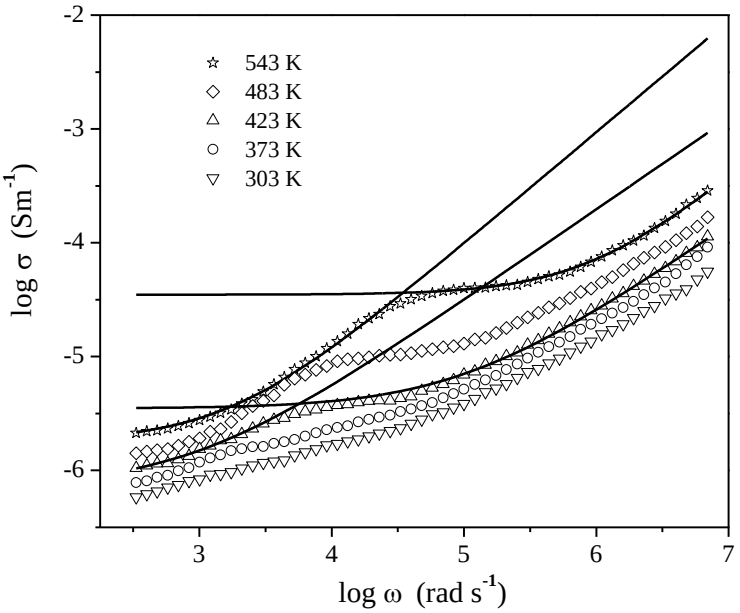

Figure 6.8 Frequency dependence of ac conductivity at different temperatures for $NiFe_2O_4/Gd_2O_3$ CSNPs

The value of s1 is found to be 0.98 at 543 K and 0.78 at 423 K and that of s2 is found to be 0.94 at 543 K and 0.8 at 423 K. The value of σ_o at 423 K is found to be 7.2×10^{-7} and 3.2×10^{-6} Sm^{-1} in the low and high frequency regions respectively, whereas at 543 K, this is found to be 1.8×10^{-6} and 3.5×10^{-5} Sm^{-1} in the low and high frequency regions respectively. The value of A1 is found to be 4.01×10^{-9} at 423 K and 1.23×10^{-9} at 543 K and the value of A2 is found to be 3.81×10^{-10} at 423 K and 9.8×10^{-11} at 543 K.

6.4 Conclusions

Gd_2O_3 encapsulated $NiFe_2O_4$ CSNPs have been synthesised by polyol method. The phase formation of the materials is confirmed by X-ray diffraction analysis. The average particle size is found to be 60 nm by Transmission electron microscope. The band gap of $NiFe_2O_4/Gd_2O_3$ CSNPs is obtained by UV-Visible absorption spectroscopy. The observed band gap of 4.38 eV lies in between the individual band gap of Gd_2O_3 and $NiFe_2O_4$. The frequency-dependent dielectric relaxation of the material is investigated in the temperature range from 303 K to 543 K. The temperature dependent relaxation times are found to obey Arrhenius law having activation energy of 0.3 eV. The Nyquist plots of impedance data are analysed by the RC equivalent circuit having a constant phase element. The dielectric relaxation is modelled by Havriliak–Negami technique in the electric modulus formalism. The frequency dependent conductivity plots follow the double power law. These investigations reveal that the crystalline phase of the core material ($NiFe_2O_4$) stabilized by the shell material (Gd_2O_3).

References

1. R. G. Chaudhuri and S. Paria, Chem. Rev. 112 (2012) 2373.
2. H. Zeng, S. Sun, J. Li, Z. L. Wang and J. P. Liu, Appl. Phys. Lett. 85 (2004) 792.
3. V. S. Maceira and M. A. C. Duarte, Adv. Mater. 19 (2007) 4131.
4. Z. L. Wang, Z. W. Quann, P. Y. Jia, C. K. Lin,, Y. Luo, Y. Chen, J. Fang, W. Zhou, C. J. O"Conner and J. Lin, Chem. Mater. 18 (2006) 2030.
5. J. Choi, T.K. Tseng, M. Davidson and P. H. Holloway, J. Mater. Chem. 21 (2011) 3113.
6. S. Mandal and K. M. Krishnan, J. Mater. Chem. 17 (2007) 372.
7. C. Langlois, D. Alloyeau, Y. L. Bouar, A. Loiseau, T. Oikawa, C. Mottet and C. Ricolleau, Faraday Discuss. 138 (2008) 375.
8. M. Younas, M. Nadeem, M. Atif and R. Grossinger, J. Appl. Phys. 109 (2011) 093704.
9. V. R. K. Murthy, Low frequency dielectric properties of ferrites (eds) V. R. K. Murthy and B. Viswanatham (Narosa Publication, New Delhi) Ch. IV (1990).
10. F. R. Sale, J. Fan and Y. T. Chien, Am. Ceram. Trans. 47 (1995) 155.
11. J. Kwo, M. Hong, A. R. Kortan, K. T. Queeney, Y. J. Chabal, J. P. Mannaerts, T. Boone, J. J. Krajewski, A. M. Sergent and J. M. Rosamilia, Appl. Phys. Lett. 77 (2000) 130.
12. J. L. Bridot, A. C. Faure, S. Laurent, C. Riviere, C. Billotey, B. Hiba, M. Janier, V. Josserand, J. L. Coll, L. Vander Elst, R. Muller, S. Roux, P. Perriat and O. Tillement, J. Am. Chem. Soc. 129 (2007) 5076.
13. R. Bazzi, M. A. Flores-Gonzalez, C. Louis, K. Lebbou, C. Dujardin, A. Brenier, W. Zhang, O. Tillement, E. Bernstein and P. Perriat, J. Lumin. 102 (2003) 445.
14. Y. Lin, L. Jiang, R. Zhao and C.W. Nan, Phys. Rev. B, 72 (2005) 014103.
15. T. K. Tseng, J. Choi, M. Davidson and P. H. Holloway, J. Mater. Chem. 20 (2010) 6115.
16. Y. W. Cao and U. J. Banin, J. Am. Chem. Soc. 122 (2000) 9692.
17. D. L. Wood and J. Tauc, Phys. Rev. B, 5 (1972) 3144.
18. X. Liu, F. Zhou, M. Gu, S. Huang, B. Liu and C. Ni, Opt. Mater. 31 (2008) 126.
19. N. Dhananjaya, H. Nagabhushana, B. M. Nagabhushana, B. Rudraswamy, S.C. Sharma, D.V. Sunitha, C. Shivakumara and R. P. S. Chakradhar, Spectrochim.

Acta Mol. Biomol. Spectros. 96 (2012) 532.

20. Q. C. Sun, H. Sims, D. Mazumdar, J. X. Ma, B. S. Holinsworth, K. R. O‟Neal, G. Kim, W. H. Butler, A. Gupta and J. L. Musfeldt, Phys. Rev. B, 86 (2012) 205106.
21. K. S. Cole and R. H. Cole, J. Chem. Phys. 9 (1941) 341.
22. D.W. Davidson and R. H. Cole, J. Chem. Phys. 19 (1951) 1484.
23. S. Havriliak and S. Negami, Polymer, 8 (1967) 161.
24. G. M. Tsangaris, G. C. Psarras and N. Kouloumbi, J. Mater. Sci. 33 (1998) 2027.
25. C. Zhao, C. Z. Zhao, M. Werner, S. Taylor and P. Chalker, Nanoscale Res. Lett. 8 (2013) 456.
26. K. Funke, Prog. Solid State Chem. 22 (1993) 111.